Disordered quantum transport in quantum anomalous Hall insulator-superconductor junctions

Jian-Xiao Zhang and Chao-Xing Liu*
Department of Physics, the Pennsylvania State University, University Park, Pennsylvania 16802, USA

(Received 20 August 2019; revised 17 August 2020; accepted 18 August 2020; published 15 October 2020)

In this work we numerically studied disordered quantum transport in a quantum anomalous Hall insulator-superconductor junction based on the effective edge model approach. In particular, we focus on the parameter regime with the mean-free path due to elastic scattering much smaller than the sample size and superconductor coherence length, and discuss disordered transport behavior in the presence of different numbers of chiral edge modes, as well as nonchiral metallic modes. Our numerical results demonstrate that the presence of multiple chiral edge modes or nonchiral metallic modes will lead to a strong Andreev conversion, giving rise to half-electron half-hole transmission through the junction structure, in sharp contrast to the suppression of Andreev conversion in the single chiral edge mode case. Our results suggest the importance of additional transport modes in the quantum anomalous Hall insulator-superconductor junction and will guide future transport measurements.

DOI: 10.1103/PhysRevB.102.144513

I. INTRODUCTION

The interplay between superconductivity proximity effect and chiral edge modes (CEMs) in a two-dimensional heterostructure with a quantum Hall (QH) or quantum anomalous Hall (QAH) system coupled to a superconductor (SC) has been a long-standing problem [1–10]. Recently, a strong resurgence of the research interest in this system results from the possible realization of a topological superconductor (TSC) phase [11]. A TSC possesses a full bulk SC gap and gapless quasiparticle excitations, such as Majorana zero modes [1,12] or parafermions [13–17], at the boundary. Non-Abelian statistics of these quasiparticle excitations enables the possibility of performing topological quantum computation based on TSC [18,19].

Early theoretical studies on the QH/SC junction focus on the Andreev reflection process occurring at the QH/SC interface [4–10] and the supercurrent flowing through CEMs [20,21]. Several early experiments on SC/semiconductor heterostructure have revealed evidence of Andreev reflections for two-dimensional electron gas in the high-Landau-level states under the magnetic fields [22–27]. Low-Landau-level states are challenging in these systems due to the limitation of the upper critical field of SCs and the high electron density [28]. Recent experiments have shown that the low-Landau-level states at a relatively low magnetic field can be achieved in the graphene system by tuning electron density through gate voltages, thus leading to significant progress in inducing SC correlation via the proximity effect into the graphene in the QH regime [8,10,29,30]. Transport evidences, including supercurrents carried by CEMs [31,32], enhanced QH plateau conductance due to Andreev process [33], cross Andreev conversion (AC) [34], and inter-Landau-level Andreev reflection [35], have been found in graphene QH systems in contact with SC electrodes under an external magnetic field. These encouraging experimental progresses lay the foundations for the theoretical proposals of realizing chiral Majorana modes (CMMs) [3,36] and Majorana zero modes [37–39] in the SC/QH (or QAH) junctions.

More recently, an observation of an $e^2/2h$ conductance kink is claimed to be the transport evidence of CMMs in the TSC phase of a QAH/SC heterostructure [11]. However, this claim is still under debate [40,41] because the early theoretical prediction was based on the calculation of the clean QAH/SC heterostructure model with the Landauer-Buttiker formalism [36] while the QAH samples in experiments, particularly the SC/QAH interface, are highly disordered [42–44]. The mean-free path l_{mfp} around the SC/QH(QAH) interface region is greatly reduced due to interface roughness and normally much smaller than the typical length scale of the SC/QH(QAH) interface. For example, in Ref. [45], l_{mfp} is around 0.3 nm, much smaller than the width of a SC ribbon (around 50–600 nm). Theoretically, the disorder effect in the SC/QH interface was investigated for the high-Landau-level systems based on either the semiclassical skipping orbit picture or the Landau level picture in the early literature [4,5,7,8]. More recently, several theoretical models are developed for the disorder-induced bulk topological phase transition in the QAH/SC heterostructures [42–44,46,47]. The disorder effect from elastic scattering is normally not important for CEM transport in the QH or QAH regime. However, the conductance oscillation can be induced by AC of CEMs propagating through the SC/QH (or QAH) interface in the ballistic regime [48,49], which is sensitive to elastic scattering. Therefore, understanding disorder effect in the SC/QH(QAH) junctions [50,51] is essential for any reliable theoretical interpretation.

In this work we focus on the disordered transport through the QAH/SC junction. We consider a theoretical model for the setup with SC partially covering the QAH system, forming a planar junction between a pure QAH region (region I) and a SC/QAH vertical junction region (region II), as shown in

*cxl56@psu.edu

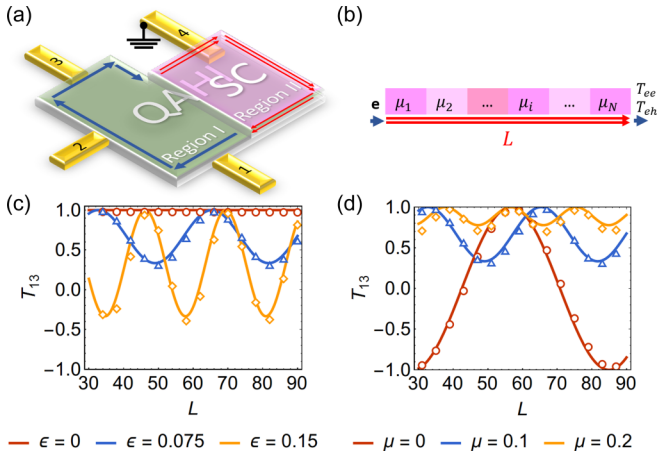

FIG. 1. (a) Schematics of the configuration for the SC-QAHI heterostructure with four leads labeled 1 to 4. (b) The trajectory of chiral edge modes going through region II in (a), which is segmented into multiple regions with local chemical potential μ_i ($i = 1, \ldots, N$). (c) The oscillation of T_{13} at a fixed chemical potential $\mu_i = \mu = 0.1t$ for different ϵ in the clean limit. (d) The oscillation of T_{13} at finite electron energy $\epsilon = 0.075t$ in the clean limit $\mu_i = \mu$ for all i. The circles, triangles, and diamonds are calculated from the microscopic model, while the solid lines are from an effective edge model.

Fig. 1(a). We assume SC proximity effect is weak in the QAH system and thus region II is topologically equivalent to the QAH phase. As a result, the CEM at the boundary of region I is transformed into two CMMs along the boundary of region II [Fig. 1(a)]. Previous theoretical studies on similar configurations have revealed a conductance oscillation [48,49] in the ballistic transport regime. We focus on the elastic-scattering-dominated transport regime, in which the edge length L of the QAH/SC junction is much larger than the mean-free path l_{mfp}. In this transport regime, the disordered transport behavior sensitively depends on the number N of CEMs and the existence of other transport channels. In the single CEM ($N = 1$) case, we find that the transmission through the boundary of QAH/SC junction region approaches unity without AC even in the presence of disorder when the incident electron energy approaches 0 (or the zero-bias limit in experiments). This is a consequence of the p-wave nature of the allowed SC proximity effect in the single CEM case. In contrast, the transmission will quickly decay away from one and reach certain saturating values when considering the finite incident electron energy (or the finite bias), or multiple CEMs ($N > 1$), or the coexistence of a CEM and a nonchiral metallic mode. These results bring new insights into the existing experiments of QAH/SC junction and reveal the important role of the interplay between elastic scattering and CMM transport.

The paper is organized as follows. In Sec. II we first discuss the model Hamiltonian and transport of a single CEM without disorder. In the next section, Sec. III, we consider the potential coupling to both the other CEMs and metallic modes under a disordered on-site chemical potential configuration. The coupling and interference effect can be manifested through measurable quantities in a realistic experimental setup, as discussed in Sec IV. Finally, the conclusion and discussion can be found in Sec. V.

II. MODEL HAMILTONIAN AND TRANSPORT OF A SINGLE CEM

Due to topological equivalence between the QH and QAH states, we consider a two-band model of QAH insulator and couple it to a SC. The Bogoliubov–de Gennes (BdG) Hamiltonian for a QAH/SC junction can be written as

$$H = \begin{pmatrix} H_{\mathrm{QAH}} & H_\Delta \\ H_\Delta^\dagger & -H_{\mathrm{QAH}}^* \end{pmatrix}, \tag{1}$$

with $H_{\mathrm{QAH}} = [M + B(\partial_x^2 + \partial_y^2)]\sigma_z + \alpha\sigma_x(-i\partial_x) + \alpha\sigma_y(-i\partial_y) - \mu$ and $\sigma_{x,y,z}$ are the Pauli matrices for spin [48]. The superconducting gap term can be described generally with $H_\Delta = i\sigma_y(\Delta_0 + \boldsymbol{d}\cdot\boldsymbol{\sigma})$, where $\boldsymbol{d} = \{d_x, d_y, d_z\}$ is a three-component vector denoting the p-wave pairing and $\boldsymbol{\sigma} = \{\sigma_x, \sigma_y, \sigma_z\}$ are the Pauli matrices. In the numerical calculation we choose $d_x = d_y = 0$, $d_z = -\Delta_x(-i\partial_x)$, which is only for demonstration purpose. In the proximity-induced SC systems with strong spin-orbit coupling and magnetization, singlet and triplet pairings are generally mixed with each other due to the absence of both time reversal symmetry and inversion symmetry [52–54]. We justify the pairing form for the current system in Appendix A.

The parameters μ, Δ_0, and Δ_x are in general spatially dependent as their values incorporate both the spatial configuration of the junctions and the disorder-induced spatial variations. We apply the Hamiltonian (1) to the configuration in Fig. 1(a) on a rectangular geometry and adopt the recursive Green's function method combined with Landauer-Büttiker formalism. The leads 1, 2, and 3 are attached on the edge of the sample. As the system possesses the particle-hole symmetry, the conservation of charge in a realistic system requires the bulk of the superconductor to be grounded, shown as lead 4 in Fig. 1(a). Leads 1 through 3 are assumed to be semi-infinite metal with the simple parabolic bands attached to the edge of the system through self-energy terms in the Green's function formalism. The calculation of Green's function allows us to obtain the full transmission matrix between all leads, without relying on knowing the detailed distribution of voltage or current. The transmission matrix combined with arbitrary current profiles on leads 1 through 3 gives the voltage distribution among all leads, as well as the four-point resistance between any two pairs of measurement leads. The physical current conservation of the entire device is automatically satisfied from the compensation of the current in lead 4. As the underlying physics is closely tied with the transmission while the experimental evidences are measured in term of resistances, we will discuss the relation in detail in Sec. IV. Details about Landauer-Büttiker formalism and the calculation of transport property can be found in Appendix E.

The system is of the total size $48a_0 \times 88a_0$. The left $30a_0 \times 88a_0$ is the QAHI region (I) and the right $18a_0 \times La_0$ is the QAHI+SC region (II), where L is the variable of system length. The rest of the system is filled with vacuum, creating the geometry shown in Fig. 1(a). Other parameters are chosen as $B = 1.5625ta_0^2$, $M = 2.625t$, $\alpha = 1.75ta_0$, $\Delta_0 = 0$, $\Delta_x = 1.2t$, $\epsilon = 0.075t$, where $a_0 \equiv 1$ is the size of unit cell and $t \equiv 1$ is the unit of energy. The parameters are extracted from a numerical projection of wave functions from the microscopic model to the edge model. A detailed comparison of the energy

spectra of both the microscopic model and the effective model is shown in Appendix B to demonstrate the validity of the approximation.

We first study the transport behavior of the Hamiltonian (1) in the clean limit and consider the transmission from lead 3 to 1, labeled as T_{13}, which accounts for the transmission through two CMMs at the boundary of region II [see Fig. 1(a)]. Through this region, electrons can transmit as an electron or convert to a hole through the AC process. We denote the electron-electron transmission as T_{ee} and the electron-hole transmission of AC as T_{eh}, thus $T_{13} = T_{ee} - T_{eh}$. In Figs. 1(c) and 1(d) the calculated T_{13} as a function of the length L is shown as circles, triangles, and diamonds for different incident electron energies ϵ and different chemical potentials μ, respectively. The oscillation behavior of transmission comes from the AC at the SC/QAH boundary [48,49]. The amplitude of the oscillation increases with ϵ (or Fermi momentum of CEMs), but decreases with μ. In the $\epsilon = 0$ case, the transmission T_{13} always keeps 1, suggesting the suppression of AC in the zero-bias limit, which is consistent with the literature [20].

Since we focus on the edge transport regime with chemical potential within the bulk gap of H_{QAH}, the full Hamiltonian of the QAH/SC junction can be projected into the subspace spanned by CEMs, giving rise to

$$H_{\mathrm{eff}} = \begin{pmatrix} v_f k - \mu & -v_\Delta k \\ -v_\Delta k & v_f k + \mu \end{pmatrix} \tag{2}$$

on the CEM basis of $|\phi_e\rangle$ and $|\phi_h\rangle$, where v_f is the Fermi velocity of CEM and v_Δ is the coefficient of the triplet pairing component. Detailed derivation of the effective model can be found in Appendix B. We notice that only the triplet component can contribute to the pairing term for CEMs [20], as guaranteed by the particle-hole symmetry. As described in Appendix C, the transmission T_{13} can be directly computed through the scattering matrix approach and given by

$$T_{13} = 1 - \frac{2\epsilon^2 v_\Delta^2 \sin^2\left(\frac{\sqrt{\epsilon^2 v_\Delta^2 + (v_f^2 - v_\Delta^2)\mu^2}}{v_f^2 - v_\Delta^2} L\right)}{\epsilon^2 v_\Delta^2 + (v_f^2 - v_\Delta^2)\mu^2}, \tag{3}$$

from which one finds T_{13} oscillates with the amplitude $\frac{2\epsilon^2 v_\Delta^2}{\epsilon^2 v_\Delta^2 + (v_f^2 - v_\Delta^2)\mu^2}$ and the period $\frac{v_f^2 - v_\Delta^2}{2\sqrt{\epsilon^2 v_\Delta^2 + (v_f^2 - v_\Delta^2)\mu^2}}$. The oscillation amplitude increases when increasing ϵ, but decreases when increasing μ, while the oscillation period decreases with increasing either ϵ or μ. The solid lines in Figs. 1(c) and 1(d) are calculated values of the transmission T_{13} from the edge model, with the projected parameters from the microscopic model. Compared with the results from the microscopic model (shown in three colored marks), the transmissions calculated from the two models coincide well with each other, showing a strong validity of the edge mode representation as the key features of the microscopic model. Thus we will focus on the analysis of the edge model hereafter.

According to Eq. (3), as the incident electron energy ϵ approaches zero, the oscillation amplitude vanishes, and thus the transmission T_{13} always stays at 1, independent of chemical potential μ. Physically the p-wave nature of the pairing in the effective edge model plays an important role. As the electron energy ϵ approaches zero, the transmissions of the electron and hole components are decoupled from each other, leading to the absence of Andreev reflection in the system, as first demonstrated in Ref. [20].

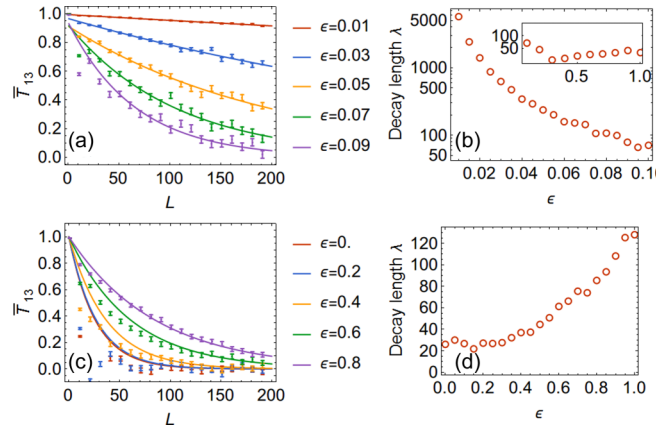

FIG. 2. (a) and (b) Single MEM case: (a) Average transmission $\bar{T}_{13}$ as a function of L for different ϵ with $\mu = 0.1$. The error bar depicts the standard error over 1000 configurations. (b) Decay length λ extracted from transmission as a function of ϵ. Other parameters are $v_f = 1ta_0$, $v_\Delta = 0.5ta_0$, $\mu_{\mathrm{imp}} = 0.5t$. Inset: The same decay length over a wider energy range $(0, 1)$, where the decaying trend continues and the decay length remains small and finite. (c) and (d) Same as (a) and (b) but for the multiple MEMs case. Other parameters are $v_{f1} = 1ta_0$, $v_{f2} = 2ta_0$, $\Delta = 0.1t$, $\mu_{\mathrm{imp}} = 1t$. The fundamental difference between the two cases is the divergence of decay length at zero energy in the single MEM case. No other singularities of decay length are observed within the energy range of interest.

More generally, the transmission oscillation is sensitive to the parameters v_f, v_Δ, and μ, which are determined by the local properties of the material. Thus, we next consider some spatial variation of the parameter values, and study how impurities and disorder in real materials would affect the measured electronic signals. As a simple case, we next consider the influence of the on-site fluctuation of chemical potential μ in the effective edge Hamiltonian (2). We will show that the introduced randomness would dramatically change the behavior of the transmission, measured in the sense of the statistical average value over random configurations.

To include randomness, we divide the QAH/SC interface into N segments labeled by the index $i = 1, 2, \ldots, N$. Within each segment, the Hamiltonian is described by Eq. (2) with a constant chemical potential μ_i, which is chosen to be a random variable from a uniform distribution on $[-\mu_{\mathrm{imp}}/2, \mu_{\mathrm{imp}}/2]$ [see Fig. 1(b)]. A configuration is generated for a given number of N. As the neighboring segments generally do not have the same chemical potentials, elastic scattering can occur at the interface of the adjacent segments. For each disorder configuration $\{\mu_i\}_{i=1,\ldots,N}$, we compute the transmission T_{13} through the transfer matrix formalism. Given a large number of identically distributed configurations, we may relate the "physical" value of transmission, denoted as $\bar{T}_{13}$, with the average value of all configurations. This averaging process is expected to induce the phase decoherence.

Figure 2(a) shows the long-distance evolution behavior of the average value $\bar{T}_{13}$, which generally reveals an exponential decay. Such decay behavior of $\bar{T}_{13}$ can be understood as

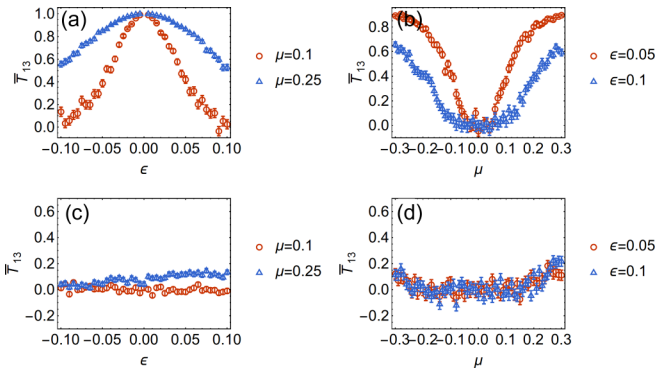

FIG. 3. (a) and (b) The energy and chemical potential dependence of the single CEM system. (c) and (d) Same as (a) and (b) but for the multiple CEMs system. System length $L = 200a_0$. The unitary transmission at zero energy of (a) causes the divergence in resistance in Fig. 6(a).

the decoherent interference between different trajectories of electron-hole oscillation when varying chemical potential. The characteristic length of such decay, denoted as λ, can be extracted from Fig. 2(a) and its dependence on ϵ is shown in Fig. 2(b). As ϵ approaches zero, λ increases rapidly, thus $\bar{T}_{13}$ almost remains 1, indicating the suppression of AC in this limit even when including disorder scattering. In a realistic experiment, both electron energy ϵ and chemical potential μ are easier to tune than the system length L. Figures 3(a) and 3(b) show how $\bar{T}_{13}$ is dependent on ϵ or μ, with a fixed system length L. The transmission $\bar{T}_{13} = 1$ at $\epsilon = 0$ for the single CEM case is immune to on-site random potential, as shown in Fig. 3(a). For a nonzero ϵ, decreasing the absolute value of μ enhances the oscillation for a single disorder configuration, leading to a faster decay to equilibrium when considering the average over multiple configurations [Fig. 3(b)].

III. DISORDERED TRANSPORT OF MULTIPLE MODES AT THE QAH/SC INTERFACE

In addition to the single CEM case discussed above, multiple transport channels can exist at the QAH/SC interface in real experiment devices, including (1) high-Landau level states with multiple CEMs ($N > 1$) for the QH states [31,34] and (2) the coexistence of a CEM and other nonchiral metallic modes [55,56]. Therefore, we next go beyond the single CEM case and study the influence of multiple modes on the disordered transport.

We first consider the case with two CEMs ($N = 2$) for simplicity. We denote the basis of the effective Hamiltonian as $\{|e_1\rangle, |e_2\rangle, |h_1\rangle, |h_2\rangle\}$, where the subscript labels two channels. In addition to the p-wave pairing between $|e_{1(2)}\rangle$ and $|h_{1(2)}\rangle$, the pairing between $|e_{1(2)}\rangle$ and $|h_{2(1)}\rangle$ also exists and can be of s-wave nature, since the electron and hole basis of two different particles are no longer constrained by particle-hole symmetry. As the linear term is induced from higher-order perturbation, we assume the leading contribution is from the constant terms. Denoting the constant pairing term as Δ, the effective Hamiltonian can be written as

$$H_{\mathrm{m}} = \begin{pmatrix} v_{f1}k - \mu_1 & 0 & 0 & \Delta \\ 0 & v_{f2}k - \mu_2 & -\Delta & 0 \\ 0 & -\Delta & v_{f1}k + \mu_1 & 0 \\ \Delta & 0 & 0 & v_{f2}k + \mu_2 \end{pmatrix}. \tag{4}$$

In Appendix D we justify this form of the Hamiltonian by considering a simple model of two chiral modes coupled to a normal SC. Unlike in the single-CEM case, the constant Δ term here is expected to induce a large oscillation in the clean limit and thus disorder can induce a strong dephasing of the oscillation pattern, giving rise to the decay behavior. This behavior has been previously studied for the QH/SC interface for the high-Landau-level QH state [4,5,7,8]. We perform transport simulations for the Hamiltonian (4) with the on-site chemical potential disorder. Figure 2(c) shows the averaged transmission $\bar{T}_{13}$ as a function of L, which shows an exponential decay with the decay length λ depending on ϵ in Fig. 2(d). In sharp contrast to the single-CEM case, the decay length does not diverge at $\epsilon = 0$ and is generally quite small for a wide range of parameter choices. As a consequence, the transmission $\bar{T}_{13}$ will be reduced close to zero for a range of ϵ and μ when the length L becomes large, as demonstrated by showing the energy and chemical potential dependence of $\bar{T}_{13}$ with a fixed system length in Figs. 3(c) and 3(d). Therefore, the behavior of the transmission $\bar{T}_{13}$ provides a clear way to distinguish between the single-CEM and multiple-CEMs cases.

We next consider the coexistence of the CEM and the nonchiral metallic mode, and this scenario has been theoretically proposed [55] and later experimentally demonstrated [56] in magnetically doped TI films. We consider the BdG Hamiltonian

$$H_{\mathrm{orig}} = \begin{pmatrix} H_{\mathrm{elec}}(k) & H_\Delta \\ H_\Delta^\dagger & -H_{\mathrm{elec}}^*(-k) \end{pmatrix}, \tag{5}$$

where

$$H_{\mathrm{elec}} = \begin{pmatrix} v_f k - \mu_1 & \xi_1 & \xi_2 \\ \xi_1 & v_1 k - \mu_2 & 0 \\ \xi_2 & 0 & -v_1 k - \mu_2 \end{pmatrix} \tag{6}$$

and

$$H_\Delta = \begin{pmatrix} 0 & \Delta_1 & \Delta_2 \\ -\Delta_1 & 0 & 0 \\ -\Delta_2 & 0 & 0 \end{pmatrix}. \tag{7}$$

Here H_{elec} is written on the basis $\{|e_c\rangle, |e_{nL}\rangle, |e_{nR}\rangle\}$, where $|e_c\rangle$ labels the CEM while $|e_{nL}\rangle$ and $|e_{nR}\rangle$ together represent the nonchiral mode due to their opposite velocities. In magnetic TI films, nonchiral modes originate from the

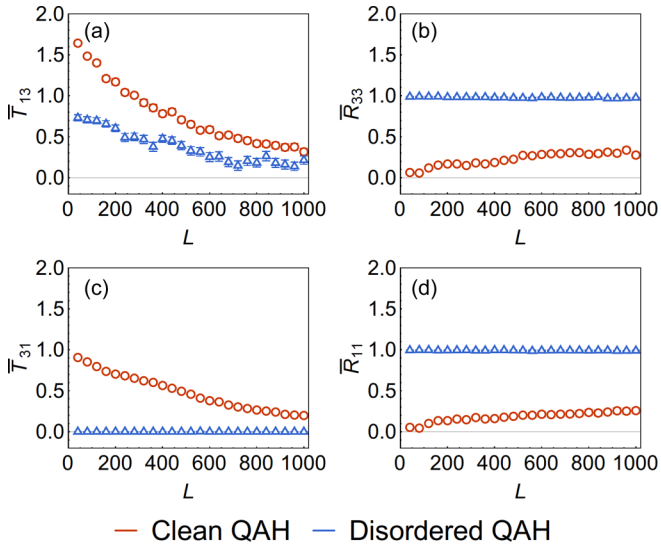

FIG. 4. Transmissions (a) and (c) and reflections (b) and (d) between leads 1 and 3 as functions of system length, for the coexistence of CEM and metallic mode case. Two different scenarios where the QAH region (region I) is clean (red) and disordered (blue) are marked. Chemical potential values are $\mu_1 = -0.3t$, $\mu_2 = -3.2t$. For details of the calculation and other parameters, please refer to Appendix E.

quasihelical gapless modes at the side surfaces of TI films [55]. The coupling between the CEM and nonchiral mode is described by the parameters $\xi_{1,2} = \xi$. The s-wave pairing gap can exist between the CEM and nonchiral mode. Here we assume the coupling between the CEM and the two nonchiral modes have the same strength $\Delta_{1,2} = \Delta$. On the other hand, the nonchiral nature also suggests the existence of backward propagating channel and thus will strongly affect the transport behavior in the QAH system [55]. The calculation involves the transmission and reflection of all six basis and the details can be found in Appendix D. To understand the influence of backward propagation, we below discuss two different scenarios, both may occur in actual experiments.

In the first scenario we assume disorder exist in the QAH/SC junction (region II) while the transport in the QAH side (region I) is ballistic (or quasiballistic), later referred as the "clean QAH" case. In this situation, the nonchiral modes have been experimentally shown to induce nonlocal transport signal in the QAH system [56]. In our setup, the ballistic transport of nonchiral modes in region I results in a negligible backscattering for $\bar{R}_{33}$ and $\bar{R}_{11}$ at small L, both saturating to certain values when increasing L in Fig. 4(b). The transmissions $\bar{T}_{13}$ and $\bar{T}_{31}$ starts from 2 and 1 for a small L, respectively, reflecting the number of the left and right moving modes. For a large L, both transmissions decay to zero in Fig. 4(a). The existence of nonzero $\bar{R}_{33}$ and $\bar{R}_{11}$ makes this situation quite different from other situations.

For the second scenario, disordered transport is assumed for the whole QAH insulator, spanning over both regions I and II in Fig. 1(a), and later referred as the "disordered QAH" case. Due to the Anderson localization, the 1D nonchiral mode is completely localized, as manifested by the reflection $\bar{R}_{33} \approx \bar{R}_{11} \approx h/e^2$ and $\bar{T}_{31} \approx 0$ in Figs. 4(b)–4(d). Even though getting localized, the nonchiral mode still mediates the AC at the QAH/SC interface [region II in Fig. 1(a)]. Consequently, the transmission $\bar{T}_{13}$ exponentially decays to zero for a large L, even when $\epsilon = 0$, making this situation more similar to the multiple CEMs case.

IV. EXPERIMENTAL RELEVANCE

Finally, we examine the behavior of resistance in the experimental setup of Fig. 1(a). It is worth noting that for a realistic physical system, a Schottky barrier can appear at the interface between a metal lead and a semiconductor, which contributes to a large contact resistance. However, since the purpose of this work is to reveal the effect of superconductor proximity on the quantum transport in the QAH state, we would make a simple assumption of a good wave function matching between the lead and the sample, corresponding to an Ohmic contact in experiments.

We consider the current driven from leads 2 to 4 and discuss the resistance $R_{24,14} \equiv -V_{14}/I_{24}$ and $R_{24,34} \equiv -V_{34}/I_{24}$ for four different cases shown in Fig. 5. (i) Figures 5(a) and 5(b): the single CEM case. (ii) Figures 5(c) and 5(d): the multiple CEMs case. (iii) Figures 5(e) and 5(f): the coexistence of the CEM and nonchiral metallic mode, with a clean QAH region. (iv) Figures 5(g) and 5(h): with a disordered QAH region. (Please see Appendix F for the resistance formula). Here we only consider the large L case ($L \sim 1000$). In case (i), both $R_{24,14}$ and $R_{24,34}$ show a unique insulating behavior

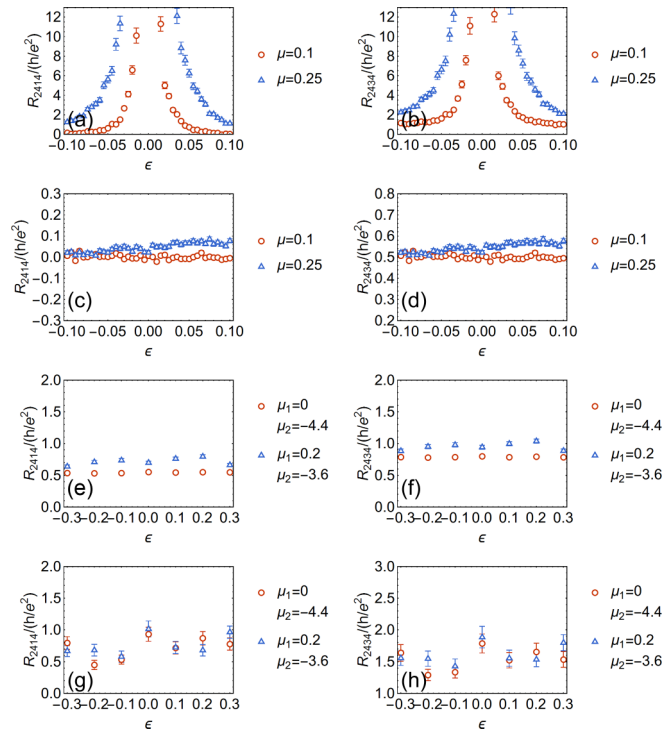

FIG. 5. Resistances $R_{24,14}$ and $R_{24,34}$ calculated from the transmission (reflection) coefficients, for the four different cases. (a) and (b) Case (i), the single CEM case. (c) and (d) Case (ii), the multiple CEMs case. (e) and (f) Case (iii), the clean QAH case with coexistence of CEM and metallic mode. (g) and (h) Case (iv), the disorder QAH case with coexistence of CEM and metallic mode.

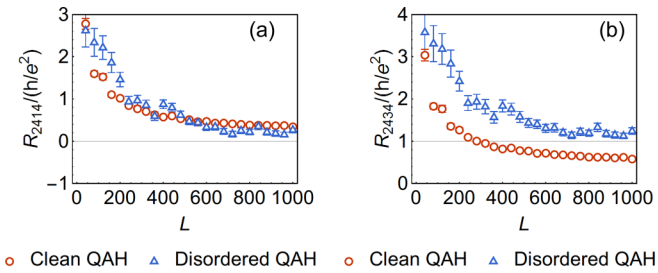

FIG. 6. (a) $R_{24,14}$ and (b) $R_{24,34}$ as functions of L for the coexistence of CEM and the metallic mode system, with red circles and blue triangles representing the clean QAH and the disordered QAH cases, respectively. For disordered QAH, the values of $R_{24,14}$ and $R_{24,34}$ saturate to 0 and h/e^2, respectively. The parameters used for (c) and (d) are $\mu_1 = -0.3t$, $\mu_2 = -3.2t$.

at $\epsilon \sim 0$ in Figs. 5(a) and 5(b), while they drop quickly to zero when ϵ is tuned away from 0. In contrast, $R_{24,14}$ and $R_{24,34}$ are insensitive to the energy ϵ for all the other cases (ii), (iii), and (iv). The values of $R_{24,14}$ and $R_{24,34}$ for cases (ii), (iii), and (iv) can be extracted from the transmission and reflection coefficients in the long L limit. We also notice that total particle probability conservation gives a simple relation between $R_{24,34}$ and $R_{24,14}$ in cases (i), (ii), and (iv). For cases (i) and (iv), $R_{24,34}$ and $R_{24,14}$ are related by $R_{24,34} - R_{24,14} = h/e^2$, while for case (ii), by $R_{24,34} - R_{24,14} = h/2e^2$, where the right-hand side is inversely proportional to the total number of transmission modes. For case (iii), due to the scattering nature of the nonchiral metallic mode, $R_{24,14}$ and $R_{24,34}$ are independent of each other. Therefore, measuring $R_{24,14}$ and $R_{24,34}$ simultaneously can distinguish these different cases.

Finally, as a comparison, we plot resistances $R_{24,14}$ and $R_{24,34}$ as a function of L for cases (iii) and (iv) in Figs. 6(a) and 6(b). The deviation of resistance summation $R_{24,34} - R_{24,14}$ from the quantized value h/e^2 differentiates the two cases. In a realistic experiment, multiple leads can be attached along the traversal side of the sample to make measurements of length dependency, and the resistance summation would allow us to determine the transport regime (ballistic or disordered) for the QAH sample.

V. CONCLUSION

Disorder and coexistence of multiple edge modes are almost inevitable in the transport measurement experiments. We showed that although the chiral edge mode is immune to the local disorder, the presence of multiple modes (either chiral or nonchiral) will lead to a strong Andreev conversion that induces a completely different transport behavior between the ballistic regime and the disordered regime. We have presented several cases where after a long distance of transmission, the saturated value of disorder-averaged conductance digress from the single chiral edge mode case where the Andreev conversion is suppressed. Our results suggest the importance of additional transport modes in the disordered quantum anomalous Hall insulator-superconductor junction and will guide the future transport experiment measurements.

ACKNOWLEDGMENTS

We are thankful for the helpful discussion with Biao Lian and Jiabin Yu. We acknowledge the support of the Office of Naval Research (Grant No. N00014-18-1-2793), the U.S. Department of Energy (Grant No. DESC0019064), and Kaufman New Initiative research grant KA2018-98553 of the Pittsburgh Foundation.

APPENDIX A: INDUCED *p*-WAVE SUPERCONDUCTING COUPLING FROM TSC

In the main text we assume a general SC coupling term containing both even and odd parity pairing. Here we show that the odd-parity pairing term can be obtained from a magnetic TI film with strong SOC in proximity to a superconductor.

We start from a BHZ-like four-band model with inversion symmetry breaking term to represent the 2D QAHI. The Hamiltonian in the basis of $\Psi_e = \{|+, e\uparrow\rangle, |-, e\uparrow\rangle, |+, e\downarrow\rangle, |-, e\downarrow\rangle\}$ can be written as

$$\Psi_e^\dagger \mathcal{H}(k)\Psi_e = \Psi_e^\dagger \begin{pmatrix} M(k)+m & U & 0 & A_2 k_- \\ U & -M(k)+m & A_2 k_+ & 0 \\ 0 & A_2 k_+ & M(k)-m & U \\ A_2 k_- & 0 & U & -M(k)-m \end{pmatrix} \Psi_e, \tag{A1}$$

where the $\pm$ in the basis denotes the orbit parity $M(k), A_2$ are model-dependent parameters, U is the asymmetric potential, m is the magnetic exchange energy, and $k_\pm = k_x \pm ik_y$. Without losing the generality, we choose the signs of parameters $M(k)$ and m so that $|+, e\downarrow\rangle$ and $|-, e\uparrow\rangle$ are the two low-energy eigenstates at $k = 0$.

When a superconductor is placed in contact with the sample, the proximity effect would create coupling between orbits of the QAHI [57–61], which may lead to complicated SC pairing form due to strong SOC. Nevertheless, we here only consider the standard s-wave singlet pairing in the four-band model. The full Hamiltonian is augmented by applying the standard BdG treatment with introducing a redundant basis set $\Psi_h = \{|+, h\uparrow\rangle, |-, h\uparrow\rangle, |+, h\downarrow\rangle, |-, h\downarrow\rangle\}$, the lowest-ordered superconducting coupling term is independent of the momentum k as

$$\Psi_h^\dagger \mathcal{H}_\Delta \Psi_e = \Psi_h^\dagger \begin{pmatrix} 0 & 0 & \Delta & 0 \\ 0 & 0 & 0 & \Delta \\ -\Delta & 0 & 0 & 0 \\ 0 & -\Delta & 0 & 0 \end{pmatrix} \Psi_e. \tag{A2}$$

The full BdG Hamiltonian reads $\mathbb{H} = \begin{pmatrix} \mathcal{H}(k) & \mathcal{H}_\Delta \\ \mathcal{H}_\Delta^\dagger & -\mathcal{H}^*(-k), \end{pmatrix}$ which can be projected into the low-energy subspace spanned by $|+, e\downarrow\rangle, |-, e\uparrow\rangle, |+, h\downarrow\rangle, |-, h\uparrow\rangle$ via the perturbation theory with the assumption that k, U, and Δ are all small numbers. Up to the third-order perturbation, one can show that an effective p-wave odd parity coupling is induced in the new Hamiltonian H [Eq. (1)] between the two projected basis. For example, the element

$$\begin{aligned}\langle -, e\uparrow|H|-, h\uparrow\rangle = &\frac{\langle -, e\uparrow|H|+, e\uparrow\rangle\langle +, e\uparrow|H|-, e\downarrow\rangle\langle -, e\downarrow|H|-, h\uparrow\rangle}{(E - E_{+,e\uparrow})(E - E_{-,e\downarrow})} \\ &+ \frac{\langle -, e\uparrow|H|+, e\downarrow\rangle\langle +, e\downarrow|H|-, e\downarrow\rangle\langle -, e\downarrow|H|-, h\uparrow\rangle}{(E - E_{+,e\downarrow})(E - E_{-,e\downarrow})} \\ &+ \frac{\langle -, e\uparrow|H|+, e\uparrow\rangle\langle +, e\uparrow|H|+, h\downarrow\rangle\langle +, h\downarrow|H|-, h\uparrow\rangle}{(E - E_{+,e\uparrow})(E - E_{+,h\downarrow})} \\ &+ \frac{\langle -, e\uparrow|H|+, e\downarrow\rangle\langle +, e\downarrow|H|+, h\uparrow\rangle\langle +, h\uparrow|H|-, h\uparrow\rangle}{(E - E_{+,e\downarrow})(E - E_{+,h\uparrow})} \\ &+ \frac{\langle -, e\uparrow|H|-, h\downarrow\rangle\langle -, h\downarrow|H|+, h\uparrow\rangle\langle +, h\uparrow|H|-, h\uparrow\rangle}{(E - E_{-,h\downarrow})(E - E_{+,h\uparrow})} \\ &+ \frac{\langle -, e\uparrow|H|-, h\downarrow\rangle\langle -, h\downarrow|H|+, h\downarrow\rangle\langle +, h\downarrow|H|-, h\uparrow\rangle}{(E - E_{-,h\downarrow})(E - E_{+,h\downarrow})} \\ &+ \text{higher order terms} \end{aligned} \tag{A3}$$

and

$$\langle(-, e\uparrow)|H|(+, h\downarrow)\rangle = 0. \tag{A4}$$

The denominators of all six terms in the third-order perturbative expression of $\langle(-, e\uparrow)|H|(-, h\uparrow)\rangle$ have the form of $UA_2k_-\Delta$ or $UA_2k_+\Delta$. For example, the first term in (A3) is

$$\frac{UA_2k_-\Delta}{(E - E_{+,e\uparrow})(E - E_{-,e\downarrow})} \propto k_- \tag{A5}$$

is linear in k. The coupling between the two lowest-energy basis, although complicated in expression, is of odd parity in nature.

APPENDIX B: DERIVATION OF THE EDGE MODEL

We choose the zero-energy solutions of H_0 with the form

$$\begin{aligned}|\gamma_1\rangle &= \frac{1}{\sqrt{2}}(u|e\uparrow\rangle + v|e\downarrow\rangle + u^*|h\uparrow\rangle + v^*|h\downarrow\rangle) \\ &\equiv \frac{1}{\sqrt{2}}(|\phi_e\rangle + |\phi_h\rangle), \end{aligned} \tag{B1}$$

$$\begin{aligned}|\gamma_2\rangle &= \frac{1}{\sqrt{2}i}(u|e\uparrow\rangle + v|e\downarrow\rangle - u^*|h\uparrow\rangle - v^*|h\downarrow\rangle) \\ &\equiv \frac{1}{\sqrt{2}i}(|\phi_e\rangle - |\phi_h\rangle), \end{aligned} \tag{B2}$$

where u and v depend on material parameters and the last set of equations define the states $|\phi_{e,h}\rangle$.

The effective edge channel Hamiltonian is constructed in the basis of $|\phi_{e,h}\rangle$ from the microscopic Hamiltonian. Consider an infinite system along the y direction, by integrating out the x dependence, the chiral edge modes with the velocity along y direction v_f lead to the terms $\langle\phi_e|H_{\text{eff}}|\phi_e\rangle = v_fk - \mu$, $\langle\phi_h|H_{\text{eff}}|\phi_h\rangle = v_fk + \mu$. Given the pairing Hamiltonian $H_\Delta = i\sigma_y\boldsymbol{d}\cdot\boldsymbol{\sigma}$, the effective pairing is given by

$$\langle\phi_e|H_\Delta|\phi_h\rangle = (u^{*2} - v^{*2})d_x + i(u^{*2} + v^{*2})d_y - 2u^*v^*d_z. \tag{B3}$$

The pairing term is determined by the detailed form of $\boldsymbol{d}$ vector. Due to the particle-hole symmetry, a constant paring term cannot appear in this basis, thus the lowest-order allowed term is linear in k. Without losing generality, we denote the pairing term as $-v_\Delta k$.

The parameter matching between the microscopic model and the edge model is done by projecting the eigenwave function of the tight-binding representation of the microscopic model on a ribbon geometry to the edge model. Figure 7

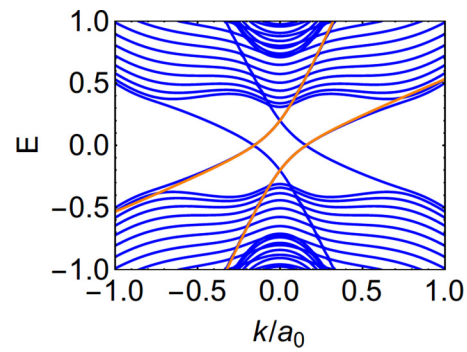

FIG. 7. The energy spectra of the microscopic model (blue, ribbon geometry with two edges) and the effective edge model (orange, single edge). The model parameters are the as in the main text, and are derived from matching the projected wave function. For the microscopic model parameters we use $B = 1.5625ta_0^2$, $M = 2.625t$, $\alpha = 1.75ta_0$, $\Delta_0 = 0$, $\Delta_x = 1.2t$, $\epsilon = 0.075t$ with the unit cell size $a_0 = 1$ and ϵ the incident electron energy. For the edge model we use $v_f = 1.75ta_0$, $v_\Delta = 1.2ta_0$, $\mu = 0.2t$.

shows a good match between the energy spectra of the microscopic model (blue lines) and the edge model (orange).

APPENDIX C: TRANSFER MATRIX METHOD FOR TRANSMISSION

In this Appendix we adopt the transfer matrix method to solve for the transmission T_{ee} and T_{eh} given a general effective Hamiltonian H_{eff}, for example Eq. (2). This discussion follows Ref. [20].

A unitary Hamiltonian needs to be constructed to maintain the conservation of transmission probability. We perform the transformation

$$\tilde{H} = J^{-1/2} H_{\text{eff}} J^{1/2}, \tag{C1}$$

where $J \equiv \partial H_{\text{eff}}/\partial k$ is the (particle) current operator. The eigenstate of Hamiltonian $\tilde{H}$, denoted by $\tilde{\Psi} \equiv J^{1/2}\Psi$, satisfies $1 = \langle\tilde{\Psi}|\tilde{\Psi}\rangle = \langle\Psi|J|\Psi\rangle$, which means the normalization of $\tilde{\Psi}$ is equivalent to the probability current conversion of Ψ. The introduction of J can simplify the expression of probability current conservation.

The wave function Ψ_L at position L is related to the initial wave function Ψ_0 by

$$\Psi_L = Q_L \Psi_0 = W \Lambda_L W^{-1} \Psi_0, \tag{C2}$$

where $\Lambda_L = \text{diag}(e^{ik_1 L}, e^{ik_2 L})$ is the evolution of the eigenstates along the edge and $W \equiv \{\tilde{\Psi}_1, \tilde{\Psi}_2\}$ is constructed by projecting the incident states onto the eigenstates of $\tilde{H} - \epsilon I$, where $\tilde{\Psi}_i$ is the eigenvector with momentum k_i and energy ϵ. W is the transformation matrix taking into account the interface scattering. The matrix Q_L is the transfer matrix relating the left and right sides of the system.

We consider the initial wave function $\Psi_0 = |e\rangle$, as the wave function is injected from a QAHI edge state. The transmission is determined entirely by the evolution of the wave function through $T = 1 - 2T_{eh}$ and $T_{eh} = |\langle h|Q_L|e\rangle|^2$. For the disordered calculations of the single and multiple CEM cases, a total 1000 configurations are used in the average.

APPENDIX D: DERIVATION OF THE EFFECTIVE COUPLING BETWEEN DIFFERENT MODES

In this Appendix we consider different modes in the QAH sample coupled to the SCs, and will demonstrate that such coupling can lead to the SC proximity that result in the pairing term between different modes in the QAH sample. To be concrete, we can consider the cases of two chiral modes coupled to a normal SC with certain hopping parameters. The Hamiltonian of this system can be written as

$$H = \begin{pmatrix} H_0 & H_c \\ H_c^\dagger & H_{sc} \end{pmatrix}, \tag{D1}$$

where

$$H_0(k) = \begin{pmatrix} v_1 k - \mu_1 & & & \\ & v_2 k - \mu_2 & & \\ & & v_1 k + \mu_1 & \\ & & & v_2 k + \mu_2 \end{pmatrix}, \tag{D2}$$

$$H_{sc}(k) = \begin{pmatrix} \frac{\hbar^2 k^2}{2m_0} - \mu_{sc} & i\Delta_0\sigma_y \\ -i\Delta_0\sigma_y & -\frac{\hbar^2 k^2}{2m_0} + \mu_{sc} \end{pmatrix}, \tag{D3}$$

and

$$H_c(k) = \begin{pmatrix} T & 0 \\ 0 & -T^* \end{pmatrix}, \tag{D4}$$

with a generic form of hopping matrix $T = t_0 + t_x\sigma_x + t_y\sigma_y + t_z\sigma_z$. For simplicity we choose $v_1 = v_2 = v$ and $\mu_1 = \mu_2 = \mu_0$ and the Hamiltonian can be written as a simple form $H_0 = vk - \mu_0\tau_z$, $H_{sc} = \xi_k\tau_z - \Delta_0\sigma_y\tau_y$, with $\xi_k = \frac{\hbar^2 k^2}{2m_0} - \mu_{sc}$ and $H_c = (t_0 + t_x\sigma_x + t_z\sigma_z)\tau_z + t_y\sigma_y$. Here σ can be viewed for spin basis and τ is for particle-hole basis. The effective model can be obtained by the second order perturbation, given by $H_{\text{eff}} = H_0 + H_c(E - H_{sc})^{-1}H_c^\dagger$. H_0 is diagonal and describes two chiral modes while the correction from $H_c(E - H_{sc})^{-1}H_c^\dagger$ can give rise to the off-diagonal coupling with the form

$$[H_c(E - H_{sc})^{-1}H_c^\dagger]_{\text{off-diagonal}} \sim \frac{\Delta_0\left(t_x^2 + t_y^2 + t_z^2 - t_0^2\right)}{(\mu_0 - \mu_{sc})^2}\sigma_y\tau_y, \tag{D5}$$

which reproduces the form in Eq. (4) in the main text. Here we have dropped the momentum dependence, which is not essential, and only keep the off-diagonal term. Similar derivation can also be applied to the coupling between the chiral edge mode and nonchiral mode, which can lead to the form in Eqs. (5)–(7) in the main text.

Equation (D5) contains the general form of both spin-active (t_x, t_y, t_z) hopping terms as well as spin-inactive term t_0. We can see that the effective off-diagonal term can be nonzero even without spin-flip terms ($t_x = t_y = t_z = 0$, $t_0 \neq 0$). Thus our result is valid for both spin-active and spin-inactive interfaces.

APPENDIX E: COEXISTENCE OF CHIRAL AND METALLIC MODE

Equation (5) represents a minimal example of a chiral mode coexisting with the nonchiral modes with one left and one right mover. The nonchiral modes can originate from the ordinary parabolic band or from the quasihelical modes at the side surface of topological insulator films. The energy dispersion for this system is shown in Fig. 8.

The introduction of backscattered mode causes the left/right boundary and incoming/outgoing modes to not coincide. Thus it is more convenient to switch from the transfer matrix picture into the scattering matrix picture where the matrix relates the incoming and outgoing states. Both the transfer matrix and the scattering matrix are 6×6 matrices, with three electron basis e, $e1$, and $e2$ and three corresponding hole basis h, $h1$, and $h2$. The transition from the Q matrix to S matrix is performed as following: First we organize the basis of the Hamiltonian in right-going/left-going blocks, such that

$$\begin{aligned}&\{\Psi_{e\to L}, \Psi_{h1\to L}, \Psi_{h\to L}, \Psi_{e1\to L}, |\Psi_{e2\leftarrow L}, \Psi_{h2\leftarrow L}\}^T \\ &\quad = Q\{\Psi_{e\to 0}, \Psi_{h1\to 0}, \Psi_{h\to 0}, \Psi_{e1\to 0}, |\Psi_{e2\leftarrow 0}, \Psi_{h2\leftarrow 0}\}^T,\end{aligned} \tag{E1}$$

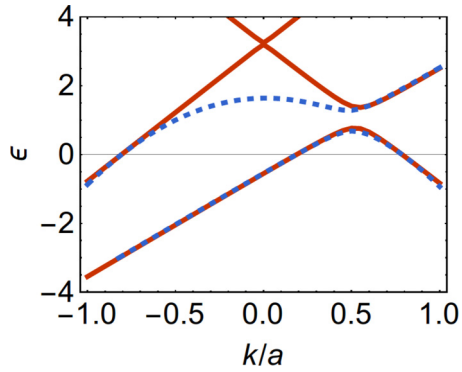

FIG. 8. (a) Red curves are the band spectra for the Hamiltonian [Eq. (6), PH partner not included] as an example to demonstrate the coexistence of CEM and a pair of helical modes. The helical modes can also approximate the spectrum of a metallic mode with a parabolic dispersion, as shown in the blue curves.

where the pipe separates the right-going and left-going modes. The above equation can be shortened as

$$\{\Psi_{\rightarrow L}, \Psi_{\leftarrow L}\}^T = Q\{\Psi_{\rightarrow 0}, \Psi_{\leftarrow 0}\}^T, \tag{E2}$$

with $\Psi_{\rightarrow(L,0)}$ and $\Psi_{\leftarrow(L,0)}$ being rank 4 and 2 spinors, respectively.

The scattering matrix on the other hand relates incoming and outgoing states, defined as

$$\{\Psi_{\leftarrow 0}, \Psi_{\rightarrow L}\}^T = S\{\Psi_{\rightarrow 0}, \Psi_{\leftarrow L}\}^T. \tag{E3}$$

The relation between the matrix S and Q can be generalized from the 2×2 case as

$$S = \begin{pmatrix} -Q^{-1}_{\leftarrow\leftarrow} Q_{\leftarrow\rightarrow} & Q^{-1}_{\leftarrow\leftarrow} \\ Q_{\rightarrow\rightarrow} - Q_{\rightarrow\leftarrow} Q^{-1}_{\leftarrow\leftarrow} Q_{\leftarrow\rightarrow} & Q_{\rightarrow\leftarrow} Q^{-1}_{\leftarrow\leftarrow} \end{pmatrix}, \tag{E4}$$

where the first (second) subscript $\leftarrow$ and $\rightarrow$ correspond to subspaces of Q with dimensions of rows (columns) of 2 and 4, respectively.

The major task is to calculate the the transmission and reflection through the QAH/SC interface, particularly the transmissions and reflections T_{13}, T_{31}, R_{11}, and R_{33} for leads 1 and 3 in our setup. Due to the coexistence of chiral and nonchiral modes in our system, we further label the chiral mode as e and h and the nonchiral modes as $e1$, $e2$ and $h1$, $h2$ where 1 and 2 denotes two opposite propagation directions, and define the transmissions and reflections between different modes as $R_{\alpha\beta}$ and $T_{\alpha\beta}$ where $\alpha, \beta = e, e1, e2, h, h1, h2$. The transmissions and reflections T_{ij} and R_{ii} $(i, j = 1, 3)$ between different leads can be related to $T_{\alpha\beta}$ and $R_{\alpha\beta}$ by

$$\begin{aligned} T_{13} &= \sum_{\alpha=e,e1} T_{\alpha,e} + T_{\alpha,e1} - T_{\alpha,h} - T_{\alpha,h1}, \\ T_{31} &= T_{e2,e2} - T_{e2,h2}, \\ R_{11} &= T_{e2,e} + T_{e2,e1} - T_{e2,h} - T_{e2,h1}, \\ R_{33} &= \sum_{\alpha=e,e1} R_{\alpha,e2} - R_{\alpha,h2}. \end{aligned} \tag{E5}$$

Furthermore, the total probability current conservation requires the conditions

$$\begin{aligned} &\sum_{i=e,e1} R_{i,e2} + R_{i,h2} + T_{i,e} + T_{i,h1} + T_{i,h} + T_{i,e1} = 2, \\ &R_{e2,e2} + R_{e2,h2} + T_{e2,e} + T_{e2,h1} + T_{e2,h} + T_{e2,e1} = 1. \end{aligned} \tag{E6}$$

Figure 9 demonstrates an example of the oscillation behavior of the 18 quantities on the left-hand side of (E6) as functions of the system length L. The unity values at $L = 0$ shows the type of incident particle of e, $e1$, and $e2$, respectively. The transmissions and reflections of incident holes are associated with the above case by PHS, and will not be further discussed. In the calculation of the total transmission/reflection from the left, we assume the ensemble of incident electrons are equally distributed between e and $e1$ channels.

With the introduction of disorder on the SC region, Figs. 10(a)–10(d) and Figs. 10(e)–10(h) show the energy ϵ dependence of the transmissions and reflections in Eq. (E5) for a given system length, for the clean QAH and disordered QAH systems, respectively. The weak dependency and lack of feature around $\epsilon = 0$ is the main difference compared with the single CEM case Figs. 3(a) and 3(b), but resemble the multiple CEMs case in Figs. 3(c) and 3(d).

The parameters used for the disordered system simulation are $v_f = 3ta_0$, $v_{f1} = -v_{f2} = 4.5ta_0$, $k_1 = 1/a_0$, $\xi = 0.3t$. In addition to the disorder on chemical potential μ, an uncorrelated random variation drawn from $[\xi_{\text{imp}}/2, \xi_{\text{imp}}/2]$ with $\xi_{\text{imp}} = 0.3t$ is also applied on the electron-coupling term ξ to obtain a shorter decay length for convenience. Qualitatively, we note that the decay and saturation of $\bar{T}_{13}$ and $\bar{R}_{33}$ still holds without the ξ disorder. For both models, a total of 100 configurations are used for deriving the average and standard error. The disordered QAH system of case (iv) is modeled as a one-dimensional system with spatial-dependent $\Delta = 0$ for $x < L_{\text{QAH}}$ and $x > L_{\text{QAH}} + L$, where the lengths of the disordered QAH section L_{QAH} is chosen to be 3500, much longer than the disorder localization length, leading to a full Anderson localization for the helical metallic mode, as shown by the schematic plot of the configuration in Fig. 9.

APPENDIX F: LANDAUER-BÜTTIKER FORMALISM IN SUPERCONDUCTOR AND DERIVATION OF RESISTANCE FROM THE TRANSMISSION COEFFICIENTS

In this Appendix we will review the general expression for Landauer-Büttiker formalism in a superconducting system [62]. In the BdG representation of the superconductor Hamiltonian, the transmission of quasiparticles between lead p and q can be calculated as

$$T^{e,h}_{pq} = \text{Tr}[\Gamma_p P^{e,h}_{pq} G \Gamma_q (P^{e,h}_{pq} G)^\dagger], \tag{F1}$$

where e, h stands for the electron/hole particle species, and P is the projection operator to project the Green's function G onto the corresponding subspace, Γ is determined by the characteristic of the lead. The total measurable transmission coefficient is obtained by $T_{pq} = T^e_{pq} - T^h_{pq}$, and the currents in different leads are related to the voltages through the

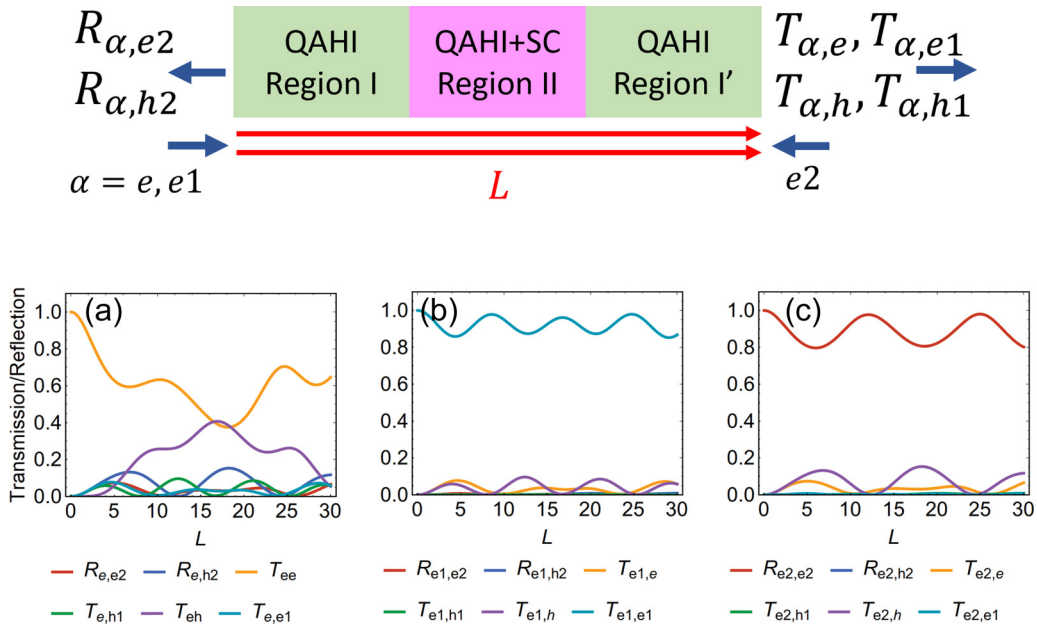

FIG. 9. A schematic figure of the effective edge model showing the three regions of disordered QAHI region (I and I′) and the QAHI+SC region (II). The incident and transmitted/reflected particles are shown as blue arrows. The CEMs are shown as red arrows. (a)–(c) An example of the 18 quantities in Eq. (E6), as functions of system length, sorted by the incident modes e, $e1$, and $e2$, respectively. The entire length of L is within region II. In (a) and (b), e and $e1$ are injected at $x = 0$, respectively, as indicated by the unitary value of the respective transmissions. For (c), $e2$ is injected at $x = L$.

transmission coefficient by

$$I_p = \sum_q T_{pq} V_q = \sum_q (T^e_{pq} - T^h_{pq}) V_q. \tag{F2}$$

We will derive the resistance of the experimental setup in the Fig. 1 in the main text from the transmissions and reflections for different cases. The transmission coefficients T_{pq} form a matrix T, which is written as a 3×3 matrix, with basis corresponding to leads 1 to 3 in Fig. 1. The voltage distribution on the leads is determined by

$$\vec{V} = T^{-1} \cdot \vec{I}, \tag{F3}$$

where both $\vec{V}$ and $\vec{I}$ are vectors of length 3, denoting the voltage and current values on leads 1 through 3. By choosing the values of components of $\vec{V}$ or $\vec{I}$, we could enforce the leads to be of constant current or constant voltage to fit our needs.

As the BdG Hamiltonian allows creation and annihilation of electron pairs, the current conservation condition in clas-

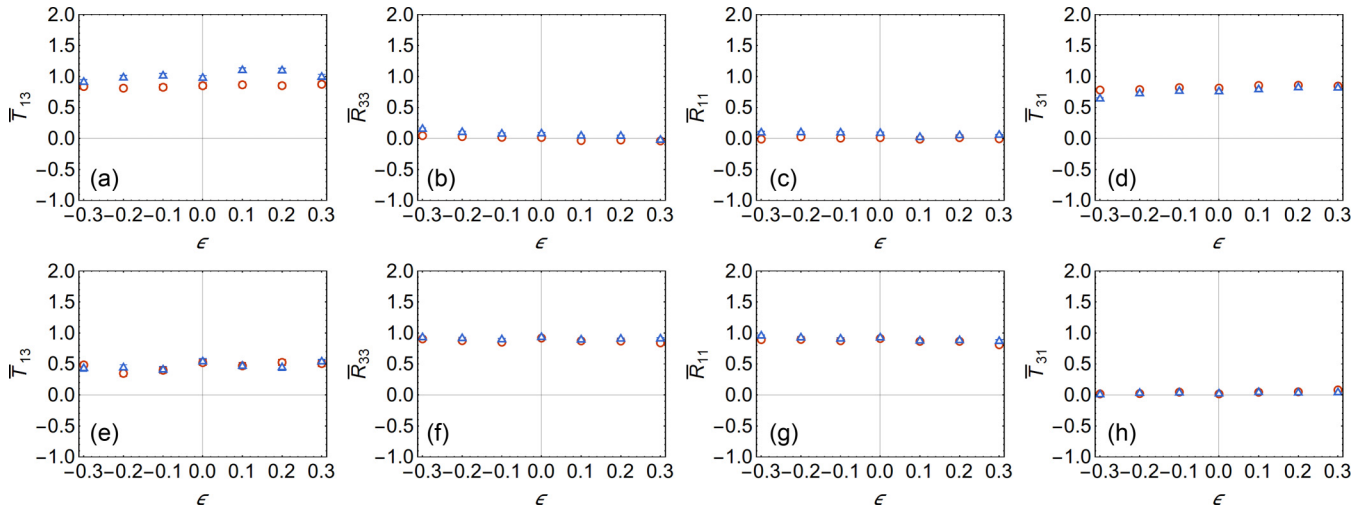

FIG. 10. The (weak) energy dependence of the forward transmission $\bar{T}_{13}$, reflection $\bar{R}_{33}$ and backward transmission $\bar{T}_{31}$, reflection $\bar{R}_{11}$ for the coexistence model. (a)–(d) The clean QAH case with system length $L = 200$. (e)–(h) The disordered QAH case with system length $L = 500$. (The values of system length are chosen to be comparable with the decay length of the corresponding systems). Red circles are for parameter set $\mu_1 = 0$, $\mu_2 = -4.4$, blue triangles are for $\mu_1 = 0.2$, $\mu_2 = -3.6$, conforming to the parameters used in Figs. 6(c) and 6(d). Contrary to the single CEM case, no significant features are present around $\epsilon \sim 0$.

sical Landauer-Büttiker formalism, manifested by the irreversibility of the matrix T, is removed. The physical explanation is that any deficiency or redundancy of current will be compensated by the ground lead from an infinite electron reservoir. Thus the current through lead 4 is implied through total current conservation.

Let us take the single CEM case as an example. The transmission matrix Eq. (F4) depends on the electronic transmission $T_{13} = T_{ee} - T_{he}$. Moreover, due to the chiral nature of the edge mode, we have $T_{21} = T_{32} = 1$ (in unit of h/e^2) and $T_{11} = T_{22} = T_{33} = -1$ followed by the standard reflection-transmission conservation. When $T_{13} = 1$, the T matrix reproduces the well-known quantum Hall case [62]. It should be noted that the transmission from lead 4 in contact with superconductors is not explicitly shown in the T matrix. However, it is implicitly required to conserve the current of the whole system [63]. Therefore, the voltage V_4 is always set to zero since the superconductor is grounded and its current is set to conserve the total current from other leads.

Once the value of transmission T is obtained, resistance can be calculated after choosing a specific voltage/current distribution. Here we always set up the current configuration and solve the voltages in different leads as a function of the currents. Let us take the example of resistance $R_{24,34} = V_{34}/I_{24}$. To evaluate this resistance, we may drive a current from lead 2 to SC body, mandating $I_{24} = I_0$, a known value of current, and further setting $I_1 = I_3 = 0$ (this means that leads 1 and 3 are voltage leads). With such current configuration of $I_{1,2,3}$, we can use the T matrix to solve all the voltages $V_{1,2,3}$. In particular, we find $V_3 = -1/(T_{13} - 1)I_0$, and thus $R_{24,34} = -1/(T_{13} - 1)$. All the other resistances can be solved numerically with the same procedure. The results are listed below.

(1) Single CEM case:

$$T = \begin{pmatrix} -1 & 0 & T_{13} \\ 1 & -1 & 0 \\ 0 & 1 & -1 \end{pmatrix}, \tag{F4}$$

$$R_{24,34} = -\frac{1}{T_{13} - 1}, \tag{F5}$$

$$R_{24,14} = -\frac{T_{13}}{T_{13} - 1}. \tag{F6}$$

(2) Multiple CEM case ($N = 2$):

$$T = \begin{pmatrix} -2 & 0 & 2T_{13} \\ 2 & -2 & 0 \\ 0 & 2 & -2 \end{pmatrix}, \tag{F7}$$

$$R_{24,34} = -\frac{1}{2(T_{13} - 1)}, \tag{F8}$$

$$R_{24,14} = -\frac{T_{13}}{2(T_{13} - 1)}. \tag{F9}$$

(3) Coexistence of CEM and nonchiral modes with the clean QAH insulator:

$$T = \begin{pmatrix} -(3 - R_{11}) & 1 & T_{13} \\ 2 & -3 & 1 \\ T_{31} & 2 & -(3 - R_{33}) \end{pmatrix}, \tag{F10}$$

$$R_{24,34} = -\frac{-2R_{11} + T_{31} + 6}{R_{11}(7 - 3R_{33}) + 7R_{33} + 3T_{13}T_{31} + 4T_{13} + T_{31} - 15}, \tag{F11}$$

$$R_{24,14} = -\frac{-R_{33} + 2T_{13} + 3}{R_{11}(7 - 3R_{33}) + 7R_{33} + 3T_{13}T_{31} + 4T_{13} + T_{31} - 15}. \tag{F12}$$

(4) Coexistence of CEM and nonchiral modes with the disordered QAH insulator:

$$T = \begin{pmatrix} -(3 - 2) & 0 & T_{13} \\ 1 & -(3 - 2) & 0 \\ 0 & 1 & -(3 - 1 - R_{33}) \end{pmatrix}, \tag{F13}$$

$$R_{24,34} = -\frac{1}{R_{33} + T_{13} - 2}, \tag{F14}$$

$$R_{24,14} = -\frac{T_{13}}{R_{33} + T_{13} - 2}. \tag{F15}$$

[1] L. Fu and C. L. Kane, Phys. Rev. Lett. **100**, 096407 (2008).
[2] L. Fu and C. L. Kane, Phys. Rev. B **79**, 161408(R) (2009).
[3] X.-L. Qi, T. L. Hughes, and S.-C. Zhang, Phys. Rev. B **82**, 184516 (2010).
[4] Y. Takagaki and K. H. Ploog, Phys. Rev. B **58**, 7162 (1998).
[5] Y. Takagaki, Phys. Rev. B **57**, 4009 (1998).
[6] H. Hoppe, U. Zülicke, and G. Schön, Phys. Rev. Lett. **84**, 1804 (2000).
[7] N. M. Chtchelkatchev and I. S. Burmistrov, Phys. Rev. B **75**, 214510 (2007).
[8] I. Khaymovich, N. Chtchelkatchev, I. Shereshevskii, and A. Mel'nikov, Europhys. Lett. **91**, 17005 (2010).

[9] Q.-f. Sun and X. Xie, J. Phys.: Condens. Matter **21**, 344204 (2009).

[10] A. R. Akhmerov and C. W. J. Beenakker, Phys. Rev. Lett. **98**, 157003 (2007).

[11] Q. L. He, L. Pan, A. L. Stern, E. C. Burks, X. Che, G. Yin, J. Wang, B. Lian, Q. Zhou, E. S. Choi *et al.*, Science **357**, 294 (2017).

[12] H.-H. Sun, K.-W. Zhang, L.-H. Hu, C. Li, G.-Y. Wang, H.-Y. Ma, Z.-A. Xu, C.-L. Gao, D.-D. Guan, Y.-Y. Li *et al.*, Phys. Rev. Lett. **116**, 257003 (2016).

[13] J. Alicea and P. Fendley, Annu. Rev. Condens. Matter Phys. **7**, 119 (2016).

[14] N. H. Lindner, E. Berg, G. Refael, and A. Stern, Phys. Rev. X **2**, 041002 (2012).

[15] A. Vaezi, Phys. Rev. X **4**, 031009 (2014).

[16] R. S. K. Mong, D. J. Clarke, J. Alicea, N. H. Lindner, P. Fendley, C. Nayak, Y. Oreg, A. Stern, E. Berg, K. Shtengel, and M. P. A. Fisher, Phys. Rev. X **4**, 011036 (2014).

[17] D. J. Clarke, J. Alicea, and K. Shtengel, Nat. Phys. **10**, 877 (2014).

[18] C. Nayak, S. H. Simon, A. Stern, M. Freedman, and S. Das Sarma, Rev. Mod. Phys. **80**, 1083 (2008).

[19] J. Alicea, Y. Oreg, G. Refael, F. Von Oppen, and M. P. Fisher, Nat. Phys. **7**, 412 (2011).

[20] J. A. M. van Ostaay, A. R. Akhmerov, and C. W. J. Beenakker, Phys. Rev. B **83**, 195441 (2011).

[21] A. Y. Zyuzin, Phys. Rev. B **50**, 323 (1994).

[22] J. Eroms, D. Weiss, J. De Boeck, G. Borghs, and U. Zülicke, Phys. Rev. Lett. **95**, 107001 (2005).

[23] T. D. Moore and D. A. Williams, Phys. Rev. B **59**, 7308 (1999).

[24] I. E. Batov, T. Schäpers, N. M. Chtchelkatchev, H. Hardtdegen, and A. V. Ustinov, Phys. Rev. B **76**, 115313 (2007).

[25] R. Frielinghaus, I. Batov, M. Weides, H. Kohlstedt, R. Calarco, and T. Schäpers, Appl. Phys. Lett. **96**, 132504 (2010).

[26] H. Takayanagi, T. Akazaki, and J. Nitta, Phys. Rev. Lett. **75**, 3533 (1995).

[27] I. Batov, T. Schäpers, A. A. Golubov, and A. Ustinov, J. Appl. Phys. **96**, 3366 (2004).

[28] Z. Wan, A. Kazakov, M. J. Manfra, L. N. Pfeiffer, K. W. West, and L. P. Rokhinson, Nat. Commun. **6**, 7426 (2015).

[29] V. Bouchiat, N. Chtchelkatchev, D. Feinberg, G. Lesovik, T. Martin, and J. Torres, Nanotechnology **14**, 77 (2002).

[30] P. Carmier, Phys. Rev. B **88**, 165415 (2013).

[31] F. Amet, C. T. Ke, I. V. Borzenets, J. Wang, K. Watanabe, T. Taniguchi, R. S. Deacon, M. Yamamoto, Y. Bomze, S. Tarucha *et al.*, Science **352**, 966 (2016).

[32] V. E. Calado, S. Goswami, G. Nanda, M. Diez, A. R. Akhmerov, K. Watanabe, T. Taniguchi, T. M. Klapwijk, and L. M. Vandersypen, Nat. Nanotechnol. **10**, 761 (2015).

[33] P. Rickhaus, M. Weiss, L. Marot, and C. Schönenberger, Nano Lett. **12**, 1942 (2012).

[34] J. Cayssol, Phys. Rev. Lett. **100**, 147001 (2008).

[35] M. R. Sahu, X. Liu, A. K. Paul, S. Das, P. Raychaudhuri, J. K. Jain, and A. Das, Phys. Rev. Lett. **121**, 086809 (2018).

[36] S. B. Chung, H.-J. Zhang, X.-L. Qi, and S.-C. Zhang, Phys. Rev. B **84**, 060510(R) (2011).

[37] C.-Z. Chen, Y.-M. Xie, J. Liu, P. A. Lee, and K. T. Law, Phys. Rev. B **97**, 104504 (2018).

[38] J. Alicea, Rep. Prog. Phys. **75**, 076501 (2012).

[39] Y. Zeng, C. Lei, G. Chaudhary, and A. H. MacDonald, Phys. Rev. B **97**, 081102(R) (2018).

[40] M. Kayyalha, D. Xiao, R. Zhang, J. Shin, J. Jiang, F. Wang, Y.-F. Zhao, L. Zhang, K. M. Fijalkowski, P. Mandal *et al.*, Science **367**, 64 (2020).

[41] P. Zhang, L. Pan, G. Yin, Q.-L. He, and K. L. Wang, arXiv:1904.12396.

[42] W. Ji and X.-G. Wen, Phys. Rev. Lett. **120**, 107002 (2018).

[43] Y. Huang, F. Setiawan, and J. D. Sau, Phys. Rev. B **97**, 100501(R) (2018).

[44] B. Lian, J. Wang, X.-Q. Sun, A. Vaezi, and S.-C. Zhang, Phys. Rev. B **97**, 125408 (2018).

[45] G.-H. Lee, K.-F. Huang, D. K. Efetov, D. S. Wei, S. Hart, T. Taniguchi, K. Watanabe, A. Yacoby, and P. Kim, Nat. Phys. **13**, 693 (2017).

[46] B. Kramer, T. Ohtsuki, and S. Kettemann, Phys. Rep. **417**, 211 (2005).

[47] J. T. Chalker, N. Read, V. Kagalovsky, B. Horovitz, Y. Avishai, and A. W. W. Ludwig, Phys. Rev. B **65**, 012506 (2001).

[48] B. Lian, J. Wang, and S.-C. Zhang, Phys. Rev. B **93**, 161401(R) (2016).

[49] O. Gamayun, J. A. Hutasoit, and V. V. Cheianov, Phys. Rev. B **96**, 241104(R) (2017).

[50] J. Wang and B. Lian, Phys. Rev. Lett. **121**, 256801 (2018).

[51] B. Lian and J. Wang, Phys. Rev. B **99**, 041404(R) (2019).

[52] L. P. Gor'kov and E. I. Rashba, Phys. Rev. Lett. **87**, 037004 (2001).

[53] E. Bauer and M. Sigrist, *Non-centrosymmetric Superconductors: Introduction and Overview* (Springer Science & Business Media, New York, 2012), Vol. 847.

[54] P. A. Frigeri, D. F. Agterberg, A. Koga, and M. Sigrist, Phys. Rev. Lett. **92**, 097001 (2004).

[55] J. Wang, B. Lian, H. Zhang, and S.-C. Zhang, Phys. Rev. Lett. **111**, 086803 (2013).

[56] C.-Z. Chang, W. Zhao, D. Y. Kim, P. Wei, J. K. Jain, C. Liu, M. H. W. Chan, and J. S. Moodera, Phys. Rev. Lett. **115**, 057206 (2015).

[57] W. McMillan, Phys. Rev. **175**, 537 (1968).

[58] T. D. Stanescu, J. D. Sau, R. M. Lutchyn, and S. Das Sarma, Phys. Rev. B **81**, 241310(R) (2010).

[59] J. D. Sau, R. M. Lutchyn, S. Tewari, and S. Das Sarma, Phys. Rev. B **82**, 094522 (2010).

[60] N. B. Kopnin and A. S. Melnikov, Phys. Rev. B **84**, 064524 (2011).

[61] I. M. Khaymovich, N. M. Chtchelkatchev, and V. M. Vinokur, Phys. Rev. B **84**, 075142 (2011).

[62] S. Datta, *Electronic Transport in Mesoscopic Systems* (Cambridge University Press, Cambridge, 1997).

[63] S. Datta, P. F. Bagwell, and M. Anantram, (1996), https://docs.lib.purdue.edu/ecetr/107/.